Front. Struct. Civ. Eng. 2025, 19(6): 946–960
https://doi.org/10.1007/s11709-025-1189-0

RESEARCH ARTICLE

Mixed mode (I/II) fracture of Glass/PA6 thermoplastic composites based on hybrid distance and correlation-based multiple target tracking methods

Seyed Aref Mousavi TEROUJENI[a], Nabi Mehri KHANSARI[a*], Hamed Danandeh HESAR[b]

[a] *Faculty of Mechanical Engineering, Sahand University of Technology, Tabriz 51335-1996, Iran*
[b] *Faculty of Biomedical Engineering, Sahand University of Technology, Tabriz 51335-1996, Iran*
[*] *Corresponding author. E-mail: n.mehri@sut.ac.ir*

ABSTRACT Conventional methods for predicting crack growth in composite materials often face limitations due to the complex nature of these materials, resulting in inaccurate predictions of crack initiation and propagation. To overcome these limitations, the research employs an advanced image processing technique to capture the behavior of GLASS/PA6 thermoplastic composites. Three algorithms (Euclidean Distance-Based Tracking Algorithm, Correlation-Based Tracking Algorithm, and Corner-Based Tracking Algorithm) are utilized to predict strain and displacement fields. The methodology involves recording displacement values through a sequence of images and applying image processing techniques to identify distinct surface features on the material. The results demonstrate strong consistency between numerical simulations and experimental data, indicating the effectiveness of this approach.

KEYWORDS mixed-mode I/II fracture, thermoplastic composite, digital image correlation method, image processing

1 Introduction

Polymer matrix composites are classified into two groups based on their behavior against temperature, thermoplastic composites and thermoset composites. Thermoplastic composites have lower chemical and thermal resistance compared to thermoset composites. Thermoplastic composites are used in various industries, with their most significant application being in the aerospace industry. A major weakness of composite materials is the initiation and growth of micro-cracks. These micro-cracks usually appear in the composite during manufacturing. Therefore, inspecting for the presence and current size of cracks, as well as their growth due to long-term loading and stress-strain application, is of great importance to engineers and designers. In the past, these strain measurements and predictions of crack growth paths in structures were carried out using traditional contact methods such as strain gauges [1–3]. On the other hand, non-contact methods for measuring strain and displacement include two main groups, interferometry methods such as laser interferometry and non-interferometric methods such as digital image correlation (DIC) [4,5]. In these methods, a uniform speckle pattern is created on the specimen. By comparing the amount of deformation of the object after loading and before loading, the amount of surface displacement (and also surface strain) of the object is obtained [4,6]. One of the advantages of the DIC method is that it can be performed with regular Light Emitting Diode (LED) and does not require a laser light source [7]. The digital image processing method has some disadvantages [7], including lower accuracy of the obtained values compared to the laser method, resolution of the image must be high and the speckle pattern on the specimen surface must be uniform. In this context, a method explored using deep neural networks (DNNs) to solve partial differential equations (PDEs). The study concludes by summarizing key results and highlighting the potential of DNN-based approaches for solving PDEs [8]. Also, a Transfer learning enhanced Physics-Informed

Article history: Received Dec 7, 2024; Accepted Mar 17, 2025

Neural Network (PINN) developed for studying the growth and propagation of crack in materials [9]. Moreover, the crack is modeled by a local enrichment of the test and trial functions with a sign function (a variant of the Heaviside step function), so that the discontinuities are along the direction of the crack [10]. A new approach was developed in which cracks allowed to be arbitrarily oriented and represented their growth by activating crack surfaces at individual particles, eliminating the need for detailed crack topology [11]. The DIC method was first proposed in the 1980s by Peter and Ranson for measuring displacements and surface strains of objects [6]. Sutton et al. [12] further developed this method in the 1980s. In recent years, DIC has been increasingly used for measuring deformation due to mechanical strain [13,14]. Sztefek et al. [15], apply this method to measure surface strains in bone under compressive loading. Zhu et al. [16] applied this method to measure thermal stresses using DIC methods. Valeri et al. [17] used this technique to predict the uniaxial stress-strain response of stainless steel. Chevalier et al. [18] used this method to obtain the strain rate of elastic materials. Quanjin et al. [19] studied and analyzed the tensile properties of aluminum materials, glass fiber-reinforced plastics, and pure resin plastics using DIC. Further, Owens and Tippur [20] measured the fracture properties of epoxy adhesives using the DIC method and the finite element method. Also, DIC method can be used for cracked printed specimens [21]. Investigating the mechanical properties of composites when cracks are present is one of the most important concerns for engineers and designers. When a crack exists in a composite body, analyzing the applied strains and, consequently, the stresses becomes more crucial because understanding the stress distribution in a cracked body aids in accurately comprehending how the crack propagates. As it was mentioned, most of the researches concentrate on investigation of mode I fracture [22–26] and mixed mode fracture [27] for isotropic or thermoset composite materials. The present literature on DIC for fracture analysis has primarily focused on thermoset composites, while thermoplastic composites, with their distinct deformation characteristics such as larger deformations and potential crushing near test fixtures, have posed challenges for accurate displacement tracking.

2 Materials and methods

2.1 Mold preparation

Silicone molds are widely recognized for their versatility and effectiveness in producing high-quality specimens. Their unique properties, such as non-stick surfaces, low shrinkage, high tensile strength, and ease of fabrication at room temperature, make them an ideal choice for various applications, including prototyping and small-scale production. In this research, silicone molds were used to produce epoxy resin specimens with three different hardener weight percentages. This finding highlights the importance of optimizing the composition of materials for specific applications. Figure 1 illustrates the epoxy resin specimens, showcasing the finishing process and notch creation using a water-jet process. The epoxy specimens were selected for their predictable and repeatable production process using silicone molds, which also served as validation specimens for image processing methods.

2.2 Glass/ PA6 preparation

The fiber and matrix volume fractions for Glass/PA6 composite specimens were determined based on ASTM D792-08 and ASTM D5630 standards. The composition was set to 60% glass fiber and 40% PA6 matrix, ensuring compliance with these widely accepted standards for material characterization [28]. The material was fabricated using the compression molding method with suitable heating process. To achieve the desired composite specimens, a custom frame was first designed and constructed. Subsequently, layers of glass fibers pre-impregnated with PA6 matrix were stacked within this frame until the required thickness was attained, as illustrated in Fig. 2(a). The frame was then subjected to pressure using a punch, following a predetermined curing schedule. Once cured, the composite sheet was cut into semicircular shapes, and notches with varying angles were created, as shown in Figs. 2(b) and 2(c).

(a) (b) (c)

Fig. 1 The epoxy resin specimens: (a) silicone mold used for producing epoxy specimens; (b) intact and notched epoxy specimens; (c) notch creation in epoxy specimens using a water-jet process.

2.3 Mixed mode (I/II) based on tracking test method

Take into account of nonlinear properties of the GLASS/PA6 thermoplastic composite, linear elastic fracture mechanics theory cannot be used [29,30]. Also, semi-circular specimen (SCB) in three-point bending tests can be used to determine the fracture toughness of pure Mode I and mixed Mode I/II in orthotropic [28] and quasi-brittle materials [31,32]. Figure 3 shows the standard SCB and its main parameters.

In Fig. 3, the S/R, a/R ratio, and β angle can be considered in such a way that different combinations of I and II failure modes are formed [33,34]. Table 1 provides the dimensions and sizes of the specimens.

Also, mechanical properties of Glass/PA6 were obtained (Table 2) according to the three points bending test set up in present SCB (Fig. 4).

The implementation and execution of the hybrid distance and Correlation-Based Multiple Target Tracking method involve three stages. The first stage is the preparation of the specimen surface and the creation of different mesh grid on it (Fig. 5). The second stage involves capturing images of the specimen surface, which includes taking an image before loading, an image during loading, and an image after loading. The final stage involves sending the captured images to the processor and processing these images.

Two types of cameras were used to capture images in this research, a digital microscope camera with up to 800x magnification and a camera with a recording rate of 240 frames per second (Fig. 6). To enhance visibility, an LED lamp was used to illuminate the specimen surface. All experiments were conducted under ambient conditions at room temperature.

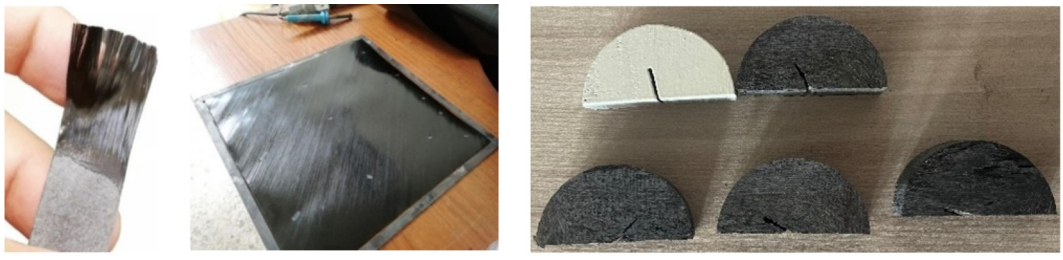

(a) (b) (c)

Fig. 2 Notched Glass/PA6 preparation steps: (a) pre-impregnated fibers with PA6 matrix; (b) pre-impregnated fibers in mold; (c) notched Glass/ PA6 specimens.

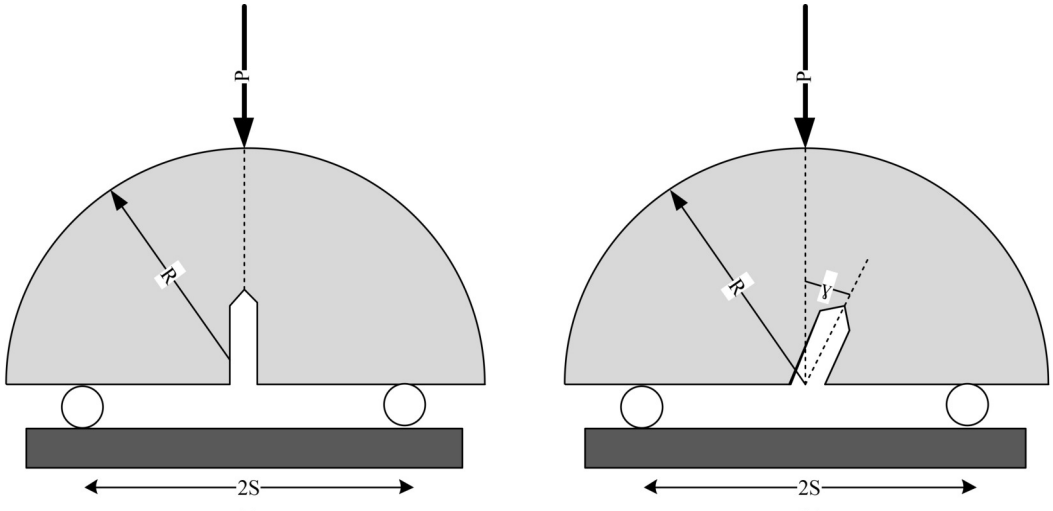

Fig. 3 The standard SCB and its main parameters: (a) pure Mode I and mixed-mode (I/II) loading conditions for the SCB specimen; (b) mixed-mode (I/II) loading conditions for the SCB specimen.

Table 1 Geometrical parameters of SCBs

Specimen's type	Loading rate (mm/min)	crack width	Notch + crack length, a	Binary distance, $2S$	Specimen thickness	Specimen radius, R
Epoxy resin	0.5	2	20 + 1.5	76.4	16	47.75
Glass/PA6	0.5	1.5	11 + 1.5	30	16	26.5

Table 2 Mechanical properties Glass/PA6 specimen

Property	Value
ν_{21}	0.036
ν_{12}	0.282
G_{23} (MPa)	2040.7
G_{12} (MPa)	2000
E_3 (MPa)	5714
E_2 (MPa)	5714
E_1 (MPa)	44160

Fig. 4 Setup for three-point bending of SCBs.

3 Theoretical and numerical analysis

The theoretical approach for speckle tracking in the DIC method is implemented with three coding algorithms. Each of these algorithms considers the tracking of a point or surface. These three algorithms include the Euclidean Distance-Based Tracking Algorithm, the Correlation-Based Tracking Algorithm and the Corner-Based Tracking Algorithm. The following figure illustrates the various stages of the process, as shown in Fig. 7.

3.1 Distance algorithm

Prior to applying the Euclidean Distance-Based Tracking Algorithm, several essential preprocessing steps were carefully performed to improve the accuracy and reliability of speckle tracking. These steps included image conversion and thresholding, where each captured image was first converted to gray scale, reducing the data to intensity values.

$$i_{\text{gray}} = 0.2989 \times R + 0.5870 \times G + 0.1140 \times B, \tag{1}$$

where R, G, and B represent the red, green, and blue color channels of the original image, respectively. Subsequently, Otsu's Thresholding method was applied to segment the image into two distinct areas, brighter regions and darker regions. Otsu's method automatically determines an optimal threshold t by maximizing the variance of gray level between the two classes,

$$t = \text{argmax}_t \sigma^2(t), \tag{2}$$

where $\sigma^2(t)$ represents the variance of the pixel intensities with threshold t. Given that the speckles were intentionally sprayed in dark tones, they were effectively segregated into the darker segment. Speckle Extraction: To isolate speckles from the background, a dual-thresholding method was used. Speckles with areas below a certain threshold, denoted as $a_{\min}$, were considered noise and removed, while those larger than another predefined threshold, $a_{\max}$, were retained.

$$a_{\min} \leqslant a_{\text{speckle}} \leqslant a_{\max}, \tag{3}$$

where a_{speckle} represents the area of a speckle. Centroid calculation, for each identified speckle blob, the centroid was calculated to serve as a reference point for subsequent tracking. The centroid c_x, c_y of a blob with n pixels, each with coordinates x_i, y_i is given as follows.

$$\begin{cases} c_x = \dfrac{1}{n}\displaystyle\sum_{i=1}^{n} x_i, \\ c_y = \dfrac{1}{n}\displaystyle\sum_{i=1}^{n} y_i, \end{cases} \tag{4}$$

these equations compute the average x and y coordinates of the pixels within the blob, yielding the centroid's position. With the centroid coordinates of each speckle-derived blob, the Euclidean Distance-Based Tracking Algorithm was employed for accurate tracking. For each image, the Euclidean Distance-Based Tracking Algorithm between each centroid and all other centroids were

(a) (b) (c)

Fig. 5 Mesh creation in Glass/PA6 specimen: (a) sprayed; (b) chess; (c) coarse grain mesh.

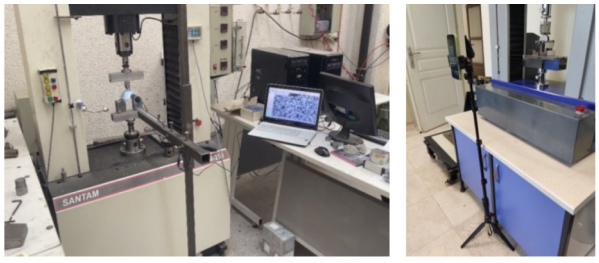

Fig. 6 Image acquisition set up: (a) digital microscope camera with up to 800× magnification; (b) 240 frames per second Camera.

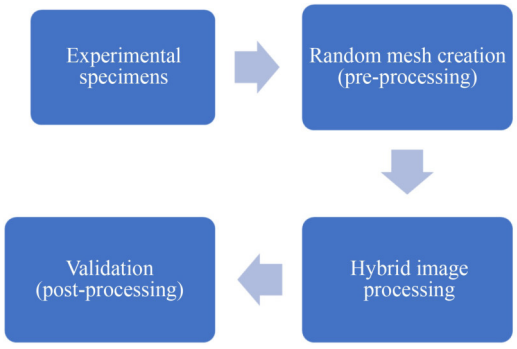

Fig. 7 Illustration of the different stages of the process.

calculated. By identifying the minimum Euclidean Distance-Based Tracking Algorithm for each centroid, we could establish accurate correspondences between speckles in consecutive frames. Specifically, for each centroid with a designated ID in the current frame, we located the nearest centroid in the subsequent frame, enabling the correct assignment of IDs to each blob in the next frame. The effectiveness of this approach is attributed to the relatively slow movement of the speckles between consecutive frames. The mathematical foundation lies in the calculation of Euclidean Distance-Based Tracking Algorithm.

$$\text{Displacement} = \sqrt{(c_{x2} - c_{x1})^2 + (c_{y2} - c_{y1})^2}, \quad (5)$$

where c_{x1}, c_{y2} and c_{x2}, c_{y2}, represent the centroid coordinates of a speckle in consecutive frames.

3.2 Correlation-Based Tracking Algorithm

Correlation-Based Tracking Algorithm is a powerful technique used for target tracking in sequential images or video frames [35]. This method involves manually selecting a region of interest (ROI) that encompasses the target in the initial image of a sequence. This selected frame, often referred to as the template, becomes the reference for tracking the target in subsequent images. The fundamental idea behind Correlation-Based Tracking Algorithm is to find the most similar region in the subsequent images that match the template, assuming that this region likely contains the target. The template, defined as the manually selected ROI in the initial image, was essentially a small image patch representing the target. This template is then compared with corresponding regions in the subsequent images using Normalized Cross-Correlation (*NCC*) to find the best match. *NCC* is the most commonly used correlation metric for this technique. It calculates the similarity between the template and the subsequent images while accounting for illumination and contrast variations. The equation for NCC is defined as follows,

$$NCC(x,y) = \frac{\sum_{i,j}\left(t(i,j) - \bar{T}\right)\left(I(i+x, j+y) - \bar{I}\right)}{\sqrt{\sum_{i,j}\left(t(i,j) - \bar{T}\right)^2 \sum_{i,j}\left(I(i+x, j+y) - \bar{I}\right)^2}}, \quad (6)$$

where $NCC(x,y)$represents the NCC value at a specific displacement (x,y) between the template T and the subsequent image I. $\bar{T}$ and $\bar{I}$ are the mean pixel intensities of the template and the corresponding region in the subsequent image, respectively. The summations are performed over all pixels within the template and the corresponding region. After calculating the *NCC* values for different displacements (x,y) the next step is to find the peak or maximum *NCC* value. This peak value indicates the most likely position of the target in the subsequent image. The process is then repeated for each subsequent image in the sequence to track the target over time. Correlation-Based Tracking Algorithm is robust to changes in target appearance, such as variations in orientation, scale, or partial occlusions. This robustness stems from the fact that the template captures the essential characteristics of the target, allowing it to be recognized even under changing conditions. One limitation of Correlation-Based Tracking Algorithm is the requirement for an initial manual selection of the target. This may not always be feasible, especially in scenarios where the target is small, fast-moving, or difficult to identify. Additionally, Correlation-Based Tracking Algorithm can be sensitive to factors like background clutter, the presence of similar objects, and rapid target movements. Correlation-Based Tracking Algorithm can be computationally intensive, especially when dealing with large search regions or high-resolution images. The computational complexity arises from the calculation of correlation values, especially when utilizing algorithms such as *NCC*. *NCC* involves intensive mathematical operations for each potential displacement of the template over the subsequent images, making it a computationally

intensive process. In the context of this research, real-time tracking may not be a primary requirement, alleviating the immediate need for rapid processing. Nonetheless, it is prudent to optimize the tracking algorithm to enhance its efficiency and performance. This can be achieved by strategically defining search areas for each tracked speckle, ensuring they are slightly larger than the associated templates. By confining the search areas to regions smaller than the original image, the algorithm's computational load is significantly reduced, leading to faster processing times. Additionally, a thoughtful selection of tracked speckles can further streamline the process. Given that the speckles near the fracture points exhibit a higher propensity for movement compared to those distant from the fracture, focusing on tracking only these relevant speckles and their associated templates becomes a viable strategy. This selective tracking approach considerably reduces computational overhead and processing time, as the algorithm concentrates on regions of higher interest.

3.3 Corner-Based Tracking Algorithm

Euclidean Distance-Based Tracking Algorithm depends on the consistent detection and segmentation of blobs. However, variations in blob size or intensity, especially when blobs are small or have low contrast with their surroundings, can hinder accurate detection and subsequent tracking.

The Harris corner detection algorithm addresses vulnerabilities in blob-based tracking by focusing on identifying corners, which are points with significant intensity changes in multiple directions. This method excels at detecting corners by analyzing local gradient changes within an image, making it robust against variations in blob size or intensity [36,37]. Harris algorithm excels at detecting corners by analyzing the local gradient changes within an image. It calculates the corner response function, denoted as R, which quantifies the corner strength at each pixel.

$$R = \det(M) - k \times \mathrm{trace}(M)^2. \tag{7}$$

The autocorrelation matrix M represents the image gradient, and k is a constant that balances the corner and edge responses. Pixels with high R values are identified as corners, indicating significant intensity changes in multiple directions, making them robust features for tracking. After identifying corners using the Harris algorithm, the next step involves tracking these corners across consecutive frames. This is accomplished by using the Euclidean Distance-Based Tracking Algorithm, as described in Subsection 3.1. Considering the definition of

Fig. 8 The element that coordinates spot number 18 with the center point.

a linear element, where the distance of each spot from a reference point is treated as an element (Fig. 8), the change in length of these elements across each frame (from start to finish of the test) can be calculated and recorded (Eqs. (8) and (9)).

Subsequently, the strain for these elements can be calculated. In other words, the strain of the elements formed by spot numbers of arbitrary points between frames can be determined. In this research, frames 1 to 137 are defined within the coordinate system (Fig. 9).

$$\Delta y_{\mathrm{target}(i)} = y_{\mathrm{target}(i)\mathrm{inframe}(n)} - y_{\mathrm{target}(i)\mathrm{inframe}(1)}, \tag{8}$$

$$\Delta x_{\mathrm{target}(i)} = x_{\mathrm{target}(i)\mathrm{inframe}(n)} - x_{\mathrm{target}(i)\mathrm{inframe}(1)}, \tag{9}$$

$$(\varepsilon_x)_{\mathrm{target}(i)} = \frac{(\Delta L_x)_{\mathrm{target}(i)}}{(L_{1x})_{\mathrm{target}(i)}} = \frac{(\Delta x)_{\mathrm{target}(i)}}{(l_{1x})_{\mathrm{target}(i)}} = \frac{\left|x_{\mathrm{inframe}(n)}\right| - \left|x_{\mathrm{inframe}(1)}\right|}{\left|x_{\mathrm{inframe}(1)}\right|}, \tag{10}$$

$$(\varepsilon_y)_{\mathrm{target}(i)} = \frac{(\Delta L_y)_{\mathrm{target}(i)}}{(L_{1y})_{\mathrm{target}(i)}} = \frac{(\Delta y)_{\mathrm{target}(i)}}{(l_{1y})_{\mathrm{target}(i)}} = \frac{\left|y_{\mathrm{inframe}(n)}\right| - \left|y_{\mathrm{inframe}(1)}\right|}{\left|y_{\mathrm{inframe}(1)}\right|}. \tag{11}$$

Another definition of strain pertains to surface strain. In this definition, the strain is considered for the surface formed by several points. The initial surface is defined as the surface formed by four arbitrary spots in the initial frame. The secondary surface is the area formed by these spots in frame. Therefore, the strain is expressed by Eq. (12), where S represents as the area.

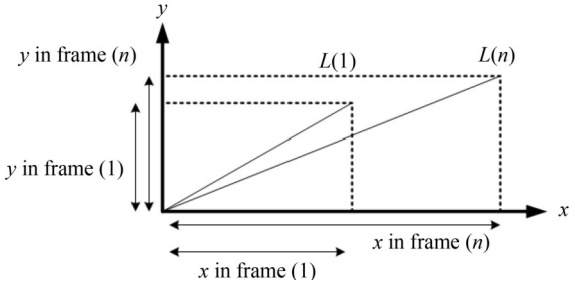

Fig. 9 Arbitrary point displacement between frames.

$$\begin{cases} \varepsilon^{x}_{\text{surface}} = \dfrac{x_{\text{in frame}(n)} - x_{\text{in frame}(1)}}{x_{\text{in frame}(1)}}, \\ \varepsilon^{y}_{\text{surface}} = \dfrac{y_{\text{in frame}(n)} - y_{\text{in frame}(1)}}{y_{\text{in frame}(1)}}. \end{cases} \tag{12}$$

Area strain values are recorded across different frames from the start to the end of the test and plotted on a graph for each specimen. These graphs are presented in the following sections. Also, the theoretical approach for obtaining mixed-mode stress intensity factors (K_{I} and K_{II}) in the notched SCB specimens can be mentioned as follows [38].

$$K_{\text{I}} = \frac{P_{\text{cr}}}{2Rt}\sqrt{\pi a} \times Y_{\text{I}}\left(\gamma, \frac{a}{R}, \frac{S}{R}\right), \tag{13}$$

$$K_{\text{II}} = \frac{P_{\text{cr}}}{2Rt}\sqrt{\pi a} \times Y_{\text{II}}\left(\gamma, \frac{a}{R}, \frac{S}{R}\right), \tag{14}$$

where a is the crack length, $2S$ is the space between the supports, and the γ is the notch angle. Also, P_{cr} is the failure load and t is the thickness of the specimen and the Y_{I} and Y_{II} are the geometric factors of mode I and II, respectively.

4 Results and discussion

4.1 Experimental result

In this study, LR630 resin and hardener (equivalent to LY5052) were used for thermoset composite. The material's hardener ratio was initially set at 30% as per the manufacturer's standard, with the flexibility to increase it up to 50%. The initial composition, which included approximately 30% to 33.33% hardener and 66.66% resin, resulted in a brittle material. This brittleness led to a high crack growth rate, making it challenging to accurately measure the displacement of elements within the material. To address this issue, the manufacturer allowed for an increase in the hardener ratio to 50%, which involves a 1:1 ratio of resin to hardener. However, as the hardener percentage approached 50%, the material became increasingly soft, with it being very soft at 50%. Through trial and error, it was determined that the optimal hardener ratio falls between 33.33% and 50%, specifically around 41.5%. At this percentage, the manufactured material exhibited suitable stiffness, allowing for the accurate tracking of element displacement prior to rupture. Figure 10 illustrates the load–displacement diagram for hardener weight ratio of 33.33%. The specimens featuring a 45° notch angle can endure up to 9.11 kN before failure, while the specimen with a 90° notch angle, made from the same material, withstands 5.24 kN before rupture. This comparison reveals that the epoxy material's resistance diminishes with an increase in the notch angle.

Figures 10(a) and 10(b) illustrate the load–displacement diagrams for epoxy resin specimens with hardener weight ratios of 33.33% and 41.5%, respectively. The specimens were prepared with notch angles of 45° and 90°, and the tests were conducted in two phases: before and after the test (as shown in Fig. 11).

As the hardener percentage approached 50%, the material became progressively softer, becoming very soft at 50%. Through trial and error, it was found that the optimal hardener ratio lies between 33.33% and 50%, specifically around 41.5%. At this ratio, the manufactured material displayed suitable stiffness, enabling accurate tracking of element displacement before rupture. Figure 12, displays the load–displacement graph for thermoplastic GLASS/PA6 composite specimens with varying notch angles.

The load–displacement diagram for the 60° notched specimen shows crack growth starting at 3.67 kN and

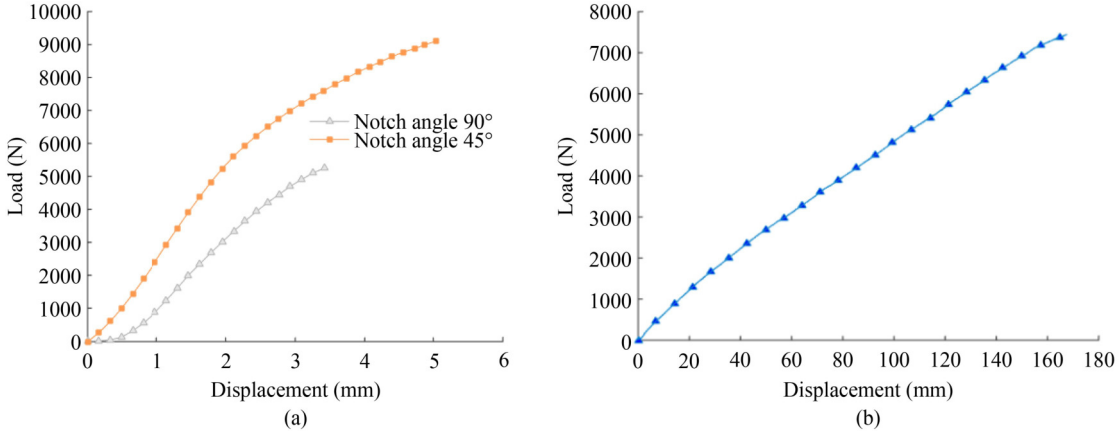

Fig. 10 Load–displacement diagrams for specimens with a notch angle of 90°, comparing epoxy resin formulations with different hardener weight ratios: (a) 33.33%; (b) 41.5%.

breaking at 4.37 kN. The 45° specimen's diagram indicates endurance up to 3.8 kN before crack growth begins, holding until 8.8 kN before complete failure. The 30° specimen experiences slight crack growth at 3.9 kN and withstands a maximum load of 4.9 kN before breaking. The 15° specimen demonstrates the highest resistance, withstanding up to 11.5 kN without crack growth before failure. Overall, the 15° notched specimen exhibits the highest resistance, while the lowest is observed in the 90° specimen. The figure reveals that most unstable crack growth occurs at displacements between 150 and 250 mm. It is concluded that increasing the notch angle generally reduces the specimens' resistance to breaking.

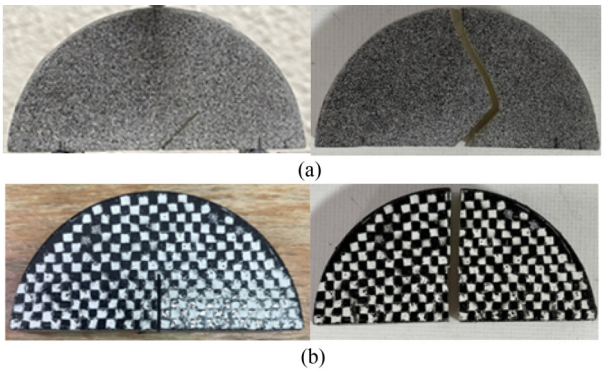

Fig. 11 Brittle epoxy resin with a hardener weight ratio of 33.33% at various notch angles: (a) notch degrees of 45°; (b) notch degrees of 90°.

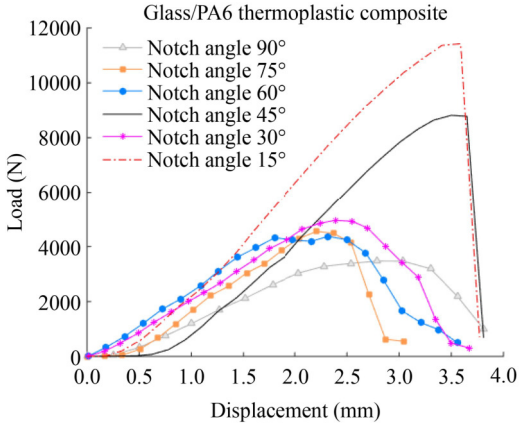

Fig. 12 Load–displacement diagram of GLASS/PA6 composites for different notch angle.

4.2 Numerical results

During the test, each spot was displaced in both the x and y directions. The displacement of these spots for each specimen was recorded. The initial coordinates of each spot were noted at the start of the test. By comparing these initial coordinates with those in the first frame, the displacement amount was determined. The tracking and calculation of spot locations in each frame were performed using three algorithms. Due to the manufacturing method of the composite sheet in this study, the fibers are aligned parallel to each other and in the same direction (unidirectional). Figure 13 illustrates the position of each spot on the specimen, labeled with its specific number, along with the quadrilateral area used to calculate the ratio of change in specimen area to the initial area, which is referred to as surface strain. This figure demonstrates the tracking procedure using the Euclidean Distance-Based Tracking Algorithm.

Figure 14 displays the quadrilaterals tracked and

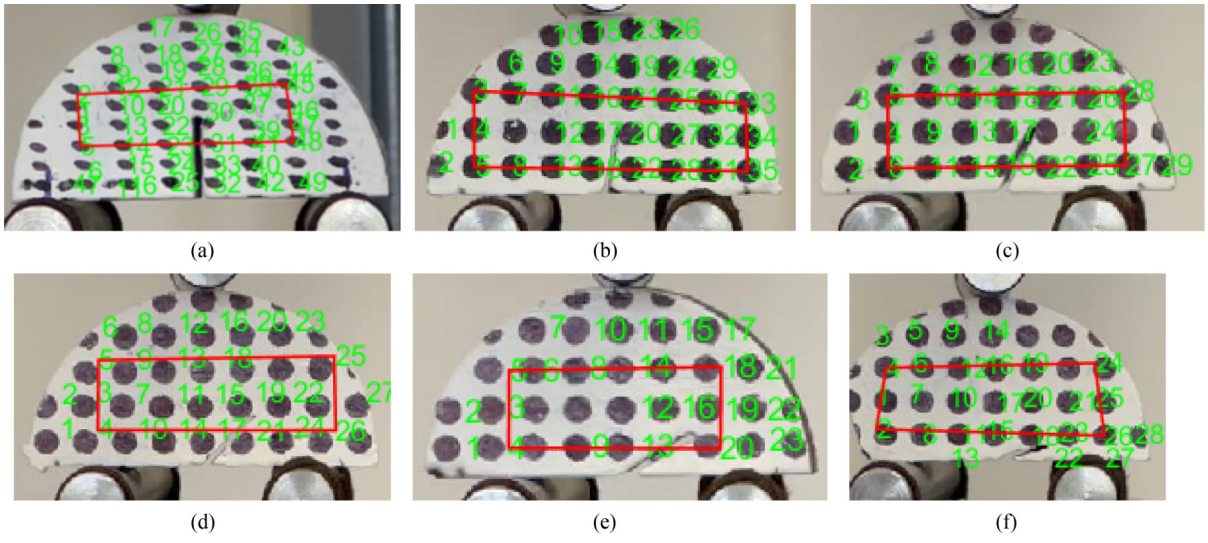

Fig. 13 The positions of specific points on a specimen, which is detected by the Euclidean Distance-Based Tracking Algorithm, and the desired quadrilateral to calculate the surface strain: (a) notch angle 90°; (b) notch angle 75°; (c) notch angle 60°; (d) notch angle 45°; (e) notch angle 30°; (f) notch angle 15°.

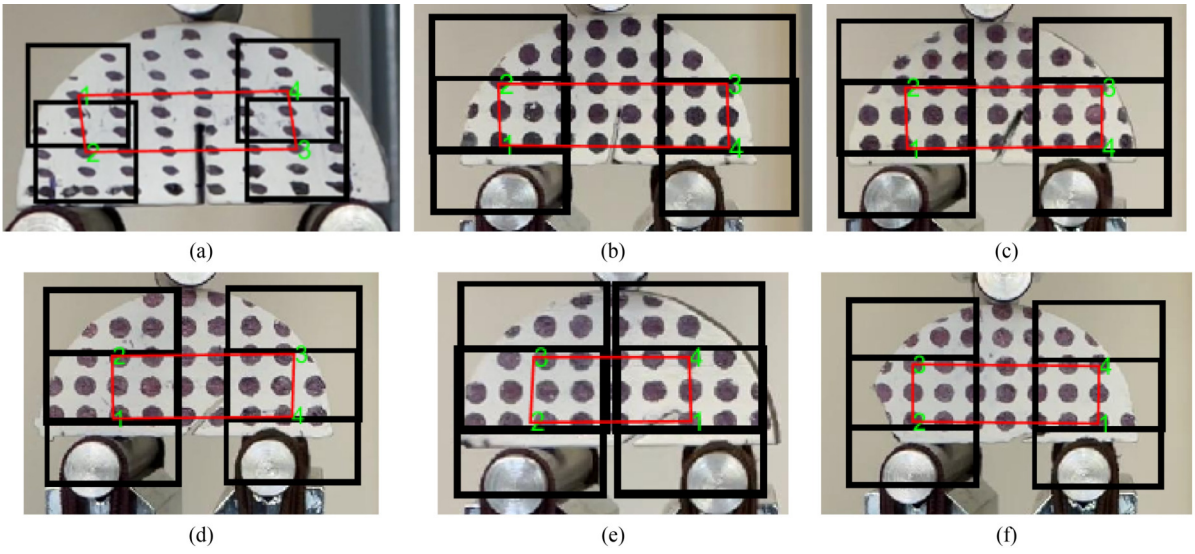

Fig. 14 The position of the quadrilaterals on the specimen that are detected by the Correlation-Based Tracking Algorithm and the desired quadrilateral to calculate the surface strain: (a) notch angle 90°; (b) notch angle 75°; (c) notch angle 60°; (d) notch angle 45°; (e) notch angle 30°; (f) notch angle 15°.

plotted using the Correlation-Based Tracking Algorithm for different specimens at the start of the test. The four points, corresponding to those selected in the Euclidean Distance-Based Tracking Algorithm, are manually chosen and connected. Subsequently, the desired surface strain for each frame will be calculated based on these quadrilaterals.

Figure 15 also illustrates the quadrilaterals obtained using the Corner-Based Tracking Algorithm.

Figure 16 displays the surface strain diagrams for each frame of the specimens. These diagrams are generated using three algorithms, each represented in different colors.

In thermoplastic materials, large deformations and surface displacements occur, requiring more advanced algorithms to track spot locations after crack propagation. Consequently, this study provides reliable measurements from the start of the test until shortly after crack initiation, while the crack size remains relatively small. The highlighted section of Fig. 17 represents the emergence and growth of microcracks (till the moment of crack initiation), which precede the development of the main crack.

As shown, all three algorithms used in this study identify three distinct regions of surface strain. Despite differences in algorithm type, crack initiation occurs in similar frames across all methods. Moreover, to validate the findings, the results from each algorithm were compared to experimental data for each notch angle. In this context, the comparison of experimental area strain

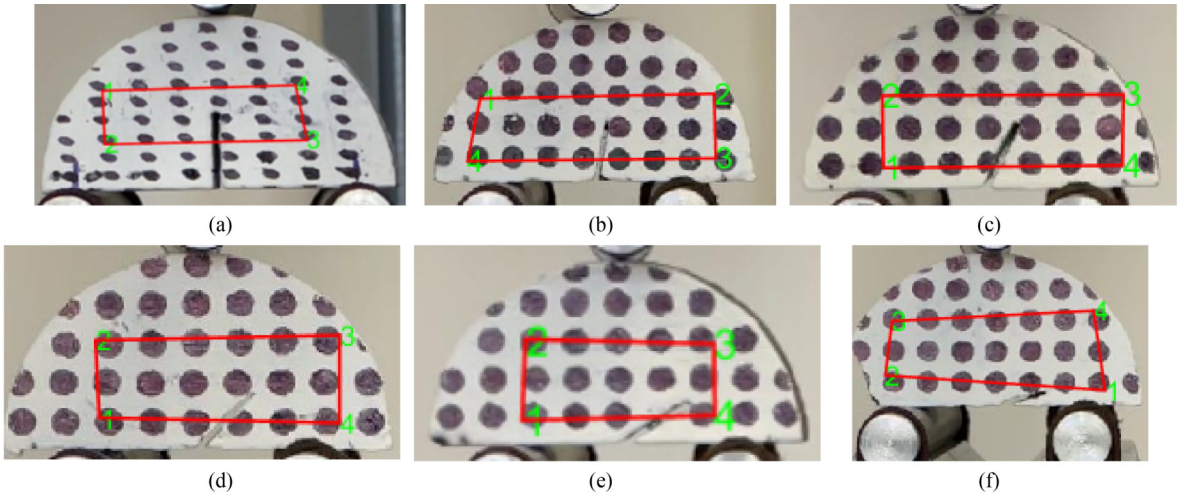

Fig. 15 The position of the four spots on the specimen that are detected by the Corner-Based Tracking Algorithm and the desired quadrilateral to calculate the surface strain: (a) notch angle 90°; (b) notch angle 75°; (c) notch angle 60°; (d) notch angle 45°; (e) notch angle 30°; (f) notch angle 15°.

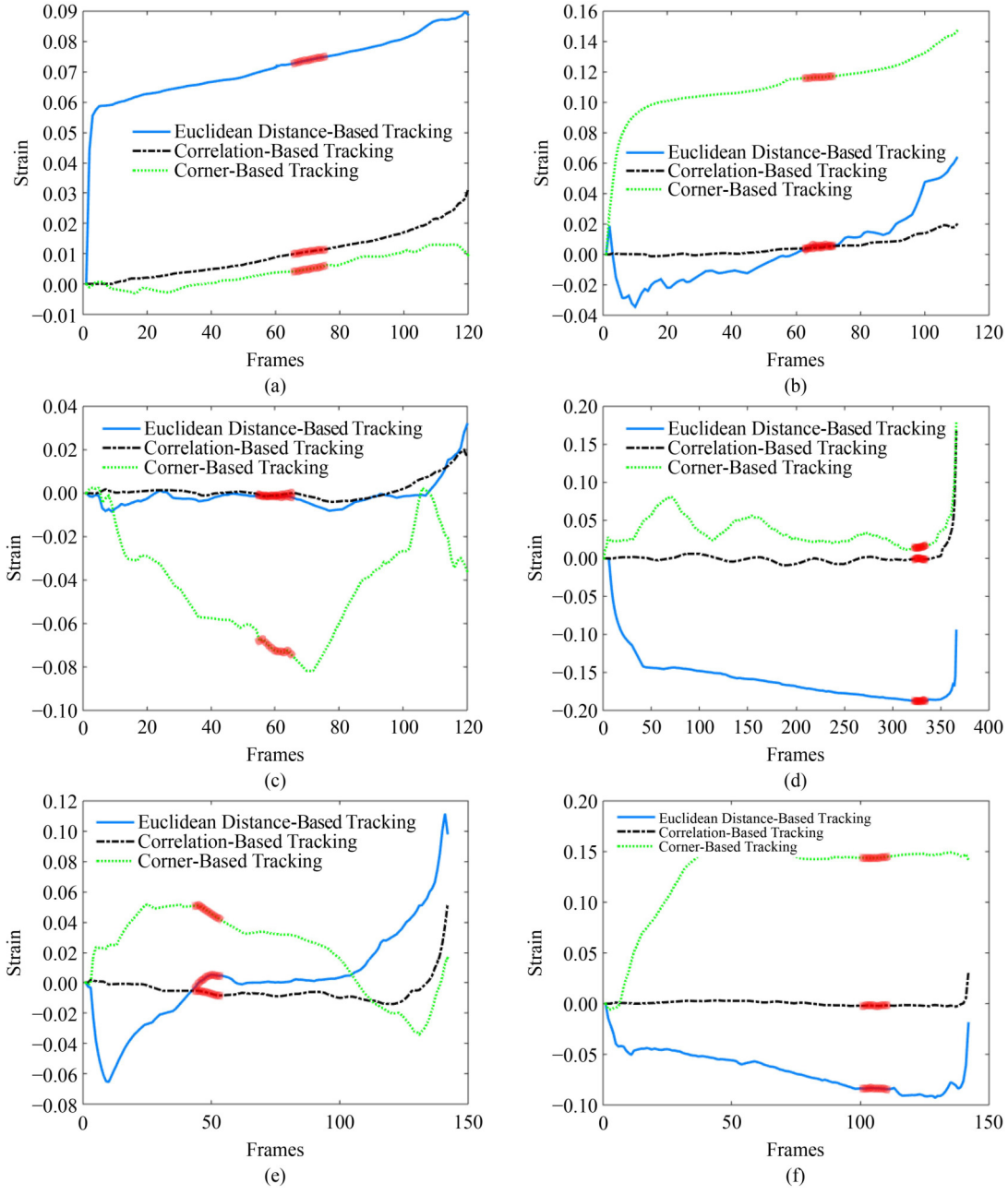

Fig. 16 The chart of surface strain value in each frame using three methods: (a) notch angle 90°; (b) notch angle 75°; (c) notch angle 60°; (d) notch angle 45°; (e) notch angle 30°; (f) notch angle 15°.

values with those calculated using three different algorithms is illustrated in following figures for notch angles ranging from 15° to 90° (Fig. 18).

The results demonstrate that at each notch angle, different algorithms align with the experimental data. This variability suggests that, unlike thermosetting materials, thermoplastic specimens require the application of specific algorithms tailored to the specimen type to accurately determine displacement and strain fields. Therefore, a single algorithm is insufficient for capturing these measurements across all conditions, emphasizing the need for algorithm selection based on material properties and experimental context. According to the results obtained, at notch angles of 15°, 30°, 60°, and 75°, the Correlation-Based Tracking and Euclidean Distance-Based Tracking Algorithms have a good agreement with the experimental results. At notch angle of 45°, all three algorithms have a good agreement with the experimental results. And at angle of 90°, the results of correlation-based tracking algorithm had a good agreement with the experimental results, although the results of Euclidean Distance-Based Tracking Algorithm can also be considered with a small percentage of error. Figure 19 illustrates the displacement path of the spots from the first

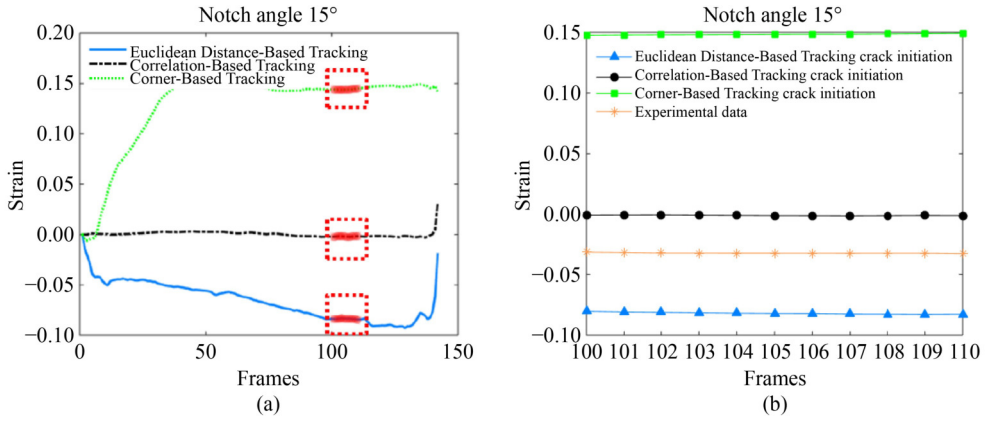

Fig. 17 Enlarged view of the microcrack initiation and growth region: (a) the microcrack initiation region; (b) the microcrack growth region.

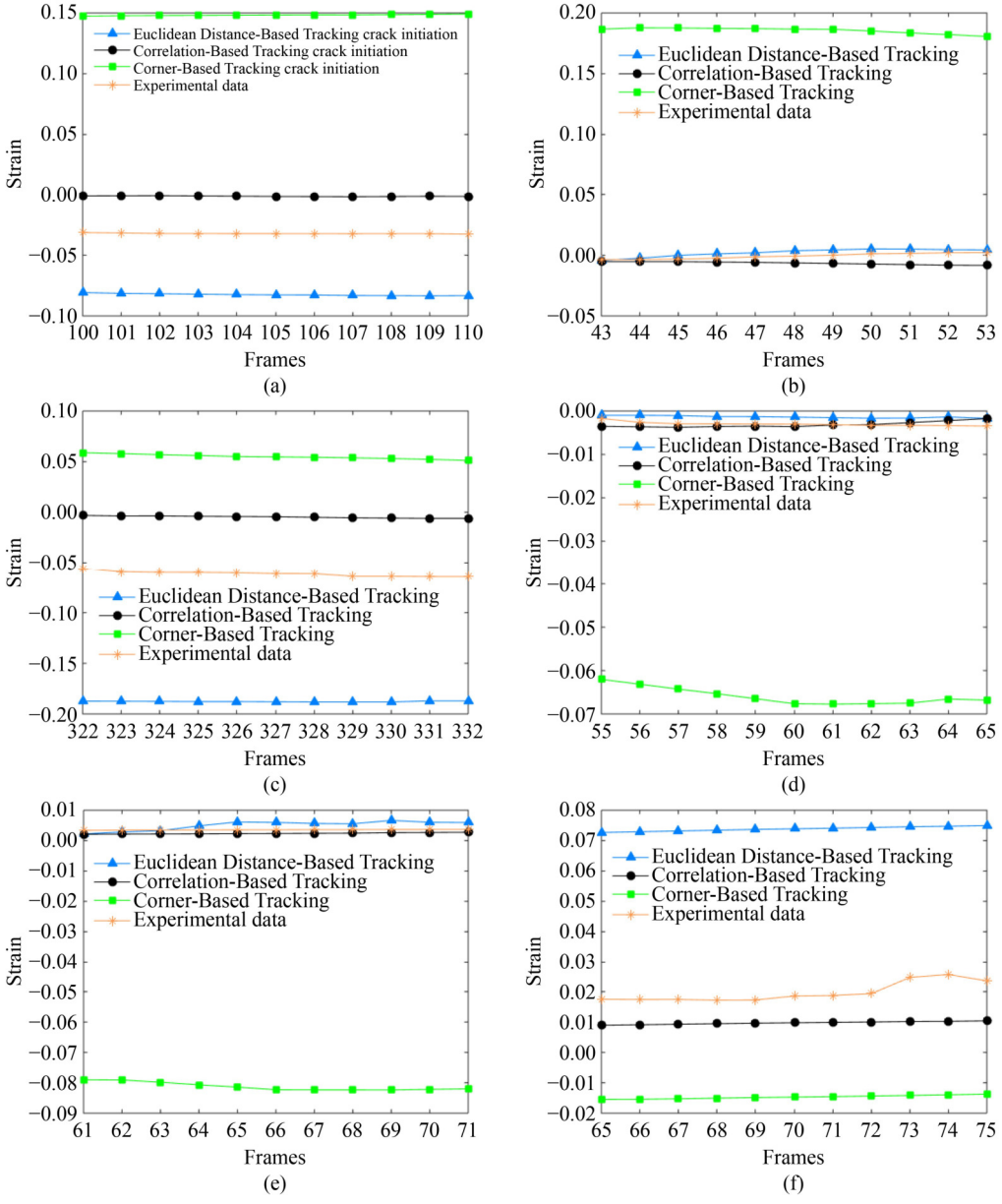

Fig. 18 Comparison of experimental area strain values with calculated strains obtained using different algorithms for notch angles ranging from 15° to 90°: (a) notch angle 15°; (b) notch angle 30°; (c) notch angle 45°; (d) notch angle 60°; (e) notch angle 75°; (f) notch angle 90°.

to the last frame for specimens with different notch angles.

As seen in Fig. 20, certain spots are labeled with numbers, but their movement trajectories are not displayed. This omission is a result of errors in the tracking algorithm for those particular spots. Table 3 presents the average displacement values for notable spots on each specimen throughout the period of crack initiation and growth, with measurements recorded in millimeters.

The table below summarizes the average surface strain results derived from the DIC method and the Euclidean Distance-Based Tracking Algorithm for multiple specimens during the crack initiation and growth phase. It is evident that most of the average strain values are negative, which is attributed to the specimen being under load and experiencing compression. Since the crack has not yet expanded, the secondary area remains smaller than the initial area. The average surface strain for various specimens is detailed in Table 4.

The graphs in Fig. 20 display the number of selected spots on the horizontal axis. The bars, colored differently,

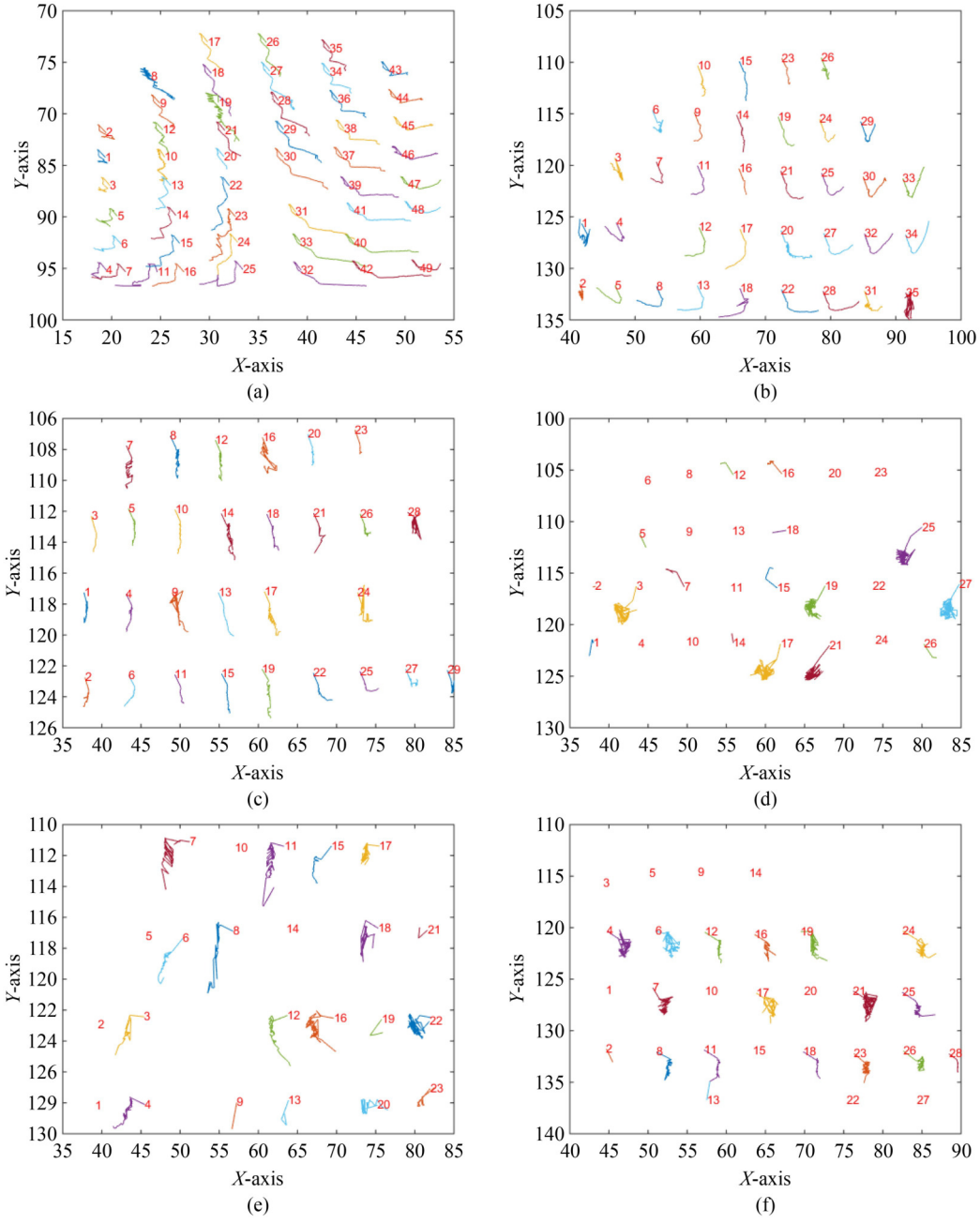

Fig. 19 The moving path of spots from the first to the last frame: (a) notch angle 90°; (b) notch angle 75°; (c) notch angle 60°; (d) notch angle 45°; (e) notch angle 30°; (f) notch angle 15°.

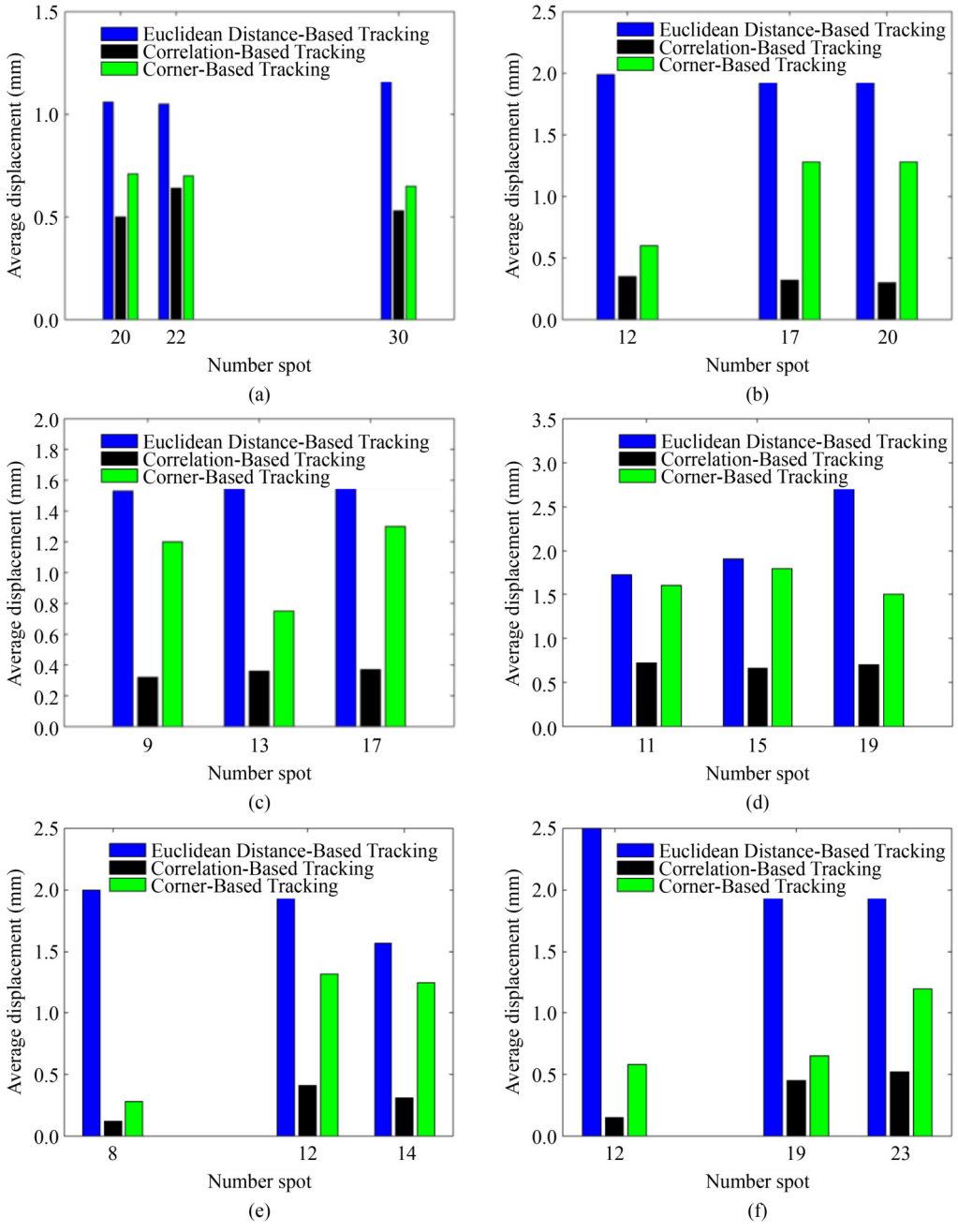

Fig. 20 The displacement values of the spots using three algorithms: (a) notch angle 90°; (b) notch angle 75°; (c) notch angle 60°; (d) notch angle 45°; (e) notch angle 30°; (f) notch angle 15°.

represent the average displacement of these spots during the crack initiation and growth phase. It is clear that the displacement values calculated using the Euclidean Distance-Based Tracking Algorithms are greater than those from the other two algorithms. Also, the Correlation-Based Tracking Algorithm yields the smallest average displacement value.

The Correlation-Based Tracking Algorithm produces displacement values that fall between those of the other two algorithms, making it a more reliable choice for calculating surface displacements of materials. Figure 21 demonstrates the planar strain results calculated using all three algorithms, with the x-axis representing the specimen types identified by their respective degrees. For each specimen, three bars in distinct colors indicate the average planar strain values computed by each algorithm. This visualization highlights the comparative performance of the algorithms in evaluating planar strain.

The Euclidean Distance-Based Tracking Algorithm yields larger values compared to the other two algorithms. Meanwhile, the results from the Correlation-Based Tracking Algorithm and the Corner-Based Tracking Algorithm are similar, showing a close proximity to each other.

Table 3 Average displacement values of significant spots on each specimen

Notch angle (°)	Number Spot	Average displacement (mm)		
		Euclidean Distance-Based Tracking	Correlation-Based Tracking	Corner-Based Tracking
90	20	1.06	0.5	0.71
	22	1.05	0.64	0.70
	30	1.42	0.53	0.65
75	12	1.99	0.358	0.600
	17	1.98	0.327	1.289
	20	2.33	0.304	1.288
60	9	1.53	0.32	1.2
	13	1.61	0.36	0.75
	17	1.93	0.37	1.3
45	11	1.73	0.72	1.6
	15	1.91	0.66	1.8
	19	3.3	0.70	1.5
30	8	2.00	0.12	0.28
	12	2.1	0.41	1.32
	14	1.57	0.31	1.25
15	12	2.5	0.15	0.58
	19	2	0.45	0.65
	23	2.1	0.52	1.2

Table 4 Average surface strain in different specimens

Specimen	Strain		
	Euclidean Distance-Based Tracking	Correlation-Based Tracking	Corner-Based Tracking
90	0.072	0.01	0.003
75	–0.0024	0.0007	0.073
60	–0.0014	–0.004	–0.06
45	–018	–0.0031	0.00045
30	0.002	–0.007	0.003
15	–0.08	–0.0012	0.04

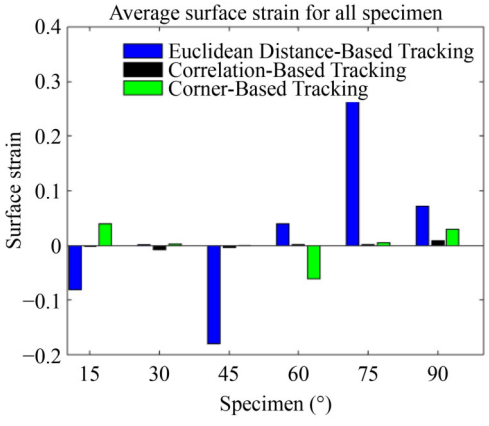

Fig. 21 Average surface strain in different specimens using three algorithms.

5 Conclusions

This study investigated the fracture behavior of semi-circular Glass/PA6 thermoplastic composites under mixed-mode (I/II) loading. Both numerical and experimental approaches were employed to achieve accurate measurements of strain and displacement in the specimens, until shortly after crack propagation. In the numerical analysis, innovative image processing techniques were developed using three distinct algorithms to predict strain and displacement fields in thermoplastic composites, which are prone to errors in traditional DIC methods. The results show that at notch angles of 15°, 30°, 60°, and 75°, both Correlation-Based Tracking and Euclidean Distance-Based Tracking Algorithms align well with experimental data. At 45°, all three algorithms have good agreement with experimental results. For a notch angle of 90°, the Correlation-Based Tracking Algorithm shows good agreement, while the Euclidean Distance-Based Tracking Algorithm also aligns well with a minor error. Overall, the Euclidean Distance algorithm yields larger values compared to the other two, which are similar to each other.

Competing interests The authors declare that they have no competing interests.

References

1. Jones R M. Mechanics of Composite Materials. Boca Raton: CRC press, 2018
2. Hartness T. Thermoplastic powder technology for advanced composite systems. Journal of Thermoplastic Composite Materials, 1988, 1(3): 210–220
3. Broggiato G B, Newaz G M, Amodio D. Application of digital speckle correlation for strain measurement in composites. Key Engineering Materials, 2001, 221–222: 337–346
4. Sirkis J S, Lim T J. Displacement and strain measurement with automated grid methods. Experimental Mechanics, 1991, 31: 382–388
5. Goldrein H T, Palmer S J P, Huntley J M. Automated fine grid technique for measurement of large-strain deformation maps. Optics and Lasers in Engineering, 1995, 23(5): 305–318
6. Peters W H, Ranson W F. Digital imaging techniques in experimental stress analysis. Optical Engineering, 1982, 21(3): 213427
7. Chu T, Ranson W, Sutton M A. Applications of digital-image-correlation techniques to experimental mechanics. Experimental Mechanics, 1985, 25: 232–244
8. Samaniego E, Anitescu C, Goswami S, Nguyen-Thanh V M, Guo H, Hamdia K, Zhuang X, Rabczuk T. An energy approach to the solution of partial differential equations in computational mechanics via machine learning: Concepts, implementation and applications. Computer Methods in Applied Mechanics and

Engineering, 2020, 362: 112790
9. Goswami S, Anitescu C, Chakraborty S, Rabczuk T. Transfer learning enhanced physics informed neural network for phase-field modeling of fracture. Theoretical and Applied Fracture Mechanics, 2020, 106: 102447
10. Rabczuk T, Belytschko T. Cracking particles: a simplified meshfree method for arbitrary evolving cracks. International Journal for Numerical Methods in Engineering, 2004, 61(13): 2316–2343
11. Rabczuk T, Belytschko T. A three-dimensional large deformation meshfree method for arbitrary evolving cracks. Computer Methods in Applied Mechanics and Engineering, 2007, 196(29–30): 2777–2799
12. Sutton M, Cheng M, Peters W, Chao Y, McNeill S. Application of an optimized digital correlation method to planar deformation analysis. Image and Vision Computing, 1986, 4(3): 143–150
13. Daiyan H, Andreassen E, Grytten F, Osnes H, Gaarder R. Shear testing of polypropylene materials analysed by digital image correlation and numerical simulations. Experimental Mechanics, 2012, 52(9): 1355–1369
14. Godara A, Raabe D. Influence of fiber orientation on global mechanical behavior and mesoscale strain localization in a short glass-fiber-reinforced epoxy polymer composite during tensile deformation investigated using digital image correlation. Composites Science and Technology, 2007, 67(11–12): 2417–2427
15. Sztefek P, Vanleene M, Olsson R, Collinson R, Pitsillides A A, Shefelbine S. Using digital image correlation to determine bone surface strains during loading and after adaptation of the mouse tibia. Journal of Biomechanics, 2010, 43(4): 599–605
16. Zhu J G, Xie H M, Li Y J, Hu Z X, Luo Q, Gu C Z. Interfacial residual stress analysis of thermal spray coatings by miniature ring-core cutting combined with DIC method. Experimental Mechanics, 2014, 54(2): 127–136
17. Valeri G, Koohbor B, Kidane A, Sutton M A. Determining the tensile response of materials at high temperature using DIC and the Virtual Fields Method. Optics and Lasers in Engineering, 2017, 91: 53–61
18. Chevalier L, Calloch S, Hild F, Marco Y. Digital image correlation used to analyze the multiaxial behavior of rubber-like materials. European Journal of Mechanics—A/Solids, 2001, 20(2): 169–187
19. Ma Q, Rejab M, Halim Q, Merzuki M, Darus M. Experimental investigation of the tensile test using digital image correlation (DIC) method. Materials Today: Proceedings, 2020, 27: 757–763
20. Owens A T, Tippur H V. Measurement of mixed-mode fracture characteristics of an epoxy-based adhesive using a hybrid digital image correlation (DIC) and finite elements (FE) approach. Optics and Lasers in Engineering, 2021, 140: 106544
21. Zekriti N, Rhanim R, Majid F, Lahlou M, Ibrahim M, Rhanim H. Mode I stress intensity factors of printed and extruded specimens based on Digital Image Correlation method (DIC): Case of ABS material. Procedia Structural Integrity, 2020, 28: 1745–1754
22. Abshirini M, Soltani N, Marashizadeh P. On the mode I fracture analysis of cracked Brazilian disc using a digital image correlation method. Optics and Lasers in Engineering, 2016, 78: 99–105
23. Moazzami M, Ayatollahi M R, Chamani H R, Guagliano M, Vergani L. Determination of higher order stress terms in cracked Brazilian disc specimen under mode I loading using digital image correlation technique. Optics and Laser Technology, 2018, 107: 344–352
24. Torabi A R, Bahrami B, Ayatollahi M R. Experimental determination of the notch stress intensity factor for sharp V-notched specimens by using the digital image correlation method. Theoretical and Applied Fracture Mechanics, 2019, 103: 102244
25. Ayatollahi M R, Moazzami M. Digital image correlation method for calculating coefficients of Williams expansion in compact tension specimen. Optics and Lasers in Engineering, 2017, 90: 26–33
26. Roux S, Hild F. Stress intensity factor measurements from digital image correlation, post-processing and integrated approaches. International Journal of Fracture, 2006, 140: 141–157
27. Zhang R, He L. Measurement of mixed-mode stress intensity factors using digital image correlation method. Optics and Lasers in Engineering, 2012, 50(7): 1001–1007
28. Ataei-Aazam M, Safarabadi M, Beygzade M, Khansari N M. Numerical & experimental assessment of mixed-modes (I/II) fracture of PMMA/hydroxyapatite nanocomposite. Theoretical and Applied Fracture Mechanics, 2023, 123: 103737
29. Hufenbach W, Langkamp A, Hornig A, Zscheyge M, Bochynek R. Analysing and modelling the 3D shear damage behaviour of hybrid yarn textile-reinforced thermoplastic composites. Composite Structures, 2011, 94(1): 121–131
30. Charitidis P. Results of finite element analysis for interlaminar fracture reinforced thermoplastic composites. Advances in Materials Science and Engineering: An International Journal, 2017, 4: 1–17
31. Ayatollahi M, Aliha M, Saghafi H. An improved semi-circular bend specimen for investigating mixed mode brittle fracture. Engineering Fracture Mechanics, 2011, 78(1): 110–123
32. Wei M D, Dai F, Xu N W, Zhao T, Xia K W. Experimental and numerical study on the fracture process zone and fracture toughness determination for ISRM-suggested semi-circular bend rock specimen. Engineering Fracture Mechanics, 2016, 154: 43–56
33. Wang H, Li H, Tang L, Zhu C, Ren X, Qiao Y, Feng G. Fracture of brittle solid with an internal penny-shaped crack: Semi-circular bending test and numerical simulation. Engineering Fracture Mechanics, 2022, 262: 108260
34. Ahmadi R, Biglari H. Presenting the traction-separation law for ultrasonic welding of glass-fiber reinforced polypropylene composite. Amirkabir Journal of Mechanical Engineering, 2022, 54(10): 2429–2456
35. Liu S, Liu D, Srivastava G, Połap D, Woźniak M. Overview and methods of correlation filter algorithms in object tracking. Complex and Intelligent Systems, 2021, 7: 1895–1917
36. Gonzalez R, Woods R. Digital Image Processing. India: Pearson education India, 2009
37. Chen J, Zou L, Zhang J, Dou L. The comparison and application of corner detection algorithms. Journal of Multimedia, 2009, 4(6): 435–441
38. Khansari N M, Aliha M R M. Mixed-modes (I/III) fracture of aluminum foam based on micromechanics of damage. International Journal of Damage Mechanics, 2023, 32(4): 519–548